RSC Advances

PAPER

View Article Online
View Journal | View Issue

Cite this: *RSC Adv.*, 2024, **14**, 16991

Characterization of chitosan- and β-cyclodextrin-modified forms of magnesium-doped hydroxyapatites as enhanced carriers for levofloxacin: loading, release, and anti-inflammatory properties

May N. Bin Jumah,[a] Sarah I. Al Othman,[a] Awatif Abdulaziz Alomari,[a] Ahmed A. Allam[bc] and Mostafa R. Abukhadra *[de]

An advanced form of magnesium-rich hydroxyapatite (Mg·HAP) was modified with two types of biopolymers, namely chitosan (CH/Mg·HAP) and β-cyclodextrin (CD/Mg·HAP), producing two types of bio-composites. The synthesized materials were developed as enhanced carriers for levofloxacin to control its loading, release, and anti-inflammatory properties. The polymeric modification significantly improved the loading efficiency to 281.4 mg g^{-1} for CH/Mg·HAP and 332.4 mg g^{-1} for CD/Mg·HAP compared with 218.3 mg g^{-1} for Mg·HAP. The loading behaviors were determined using conventional kinetic and isotherm models and mathematical parameters of new equilibrium models (the monolayer model of one energy). The estimated density of effective loading sites ($N_{m\ (LVX)}$ = 88.03 mg g^{-1} (Mg·HAP), 115.8 mg g^{-1} (CH/Mg·HAP), and 138.5 mg g^{-1} (CD/Mg·HAP)) illustrates the markedly higher loading performance of the modified forms of Mg·HAP. Moreover, the loading energies (<40 kJ mol^{-1}) in conjunction with the capacity of each loading site (n > 1) and Gaussian energies (<8 kJ mol^{-1}) signify the physical trapping of LVX molecules in vertical orientation. The addressed materials validate prolonged and continuous release behaviors. These behaviors accelerated after the modification procedures, as the complete release was identified after 160 h (CH/Mg·HAP) and 200 h (CD/Mg·HAP). The releasing behaviors are regulated by both diffusion and erosion mechanisms, according to the kinetic investigations and diffusion exponent analysis (>0.45). The entrapping of LVX into Mg·HAP induces its anti-inflammatory properties against the generation of cytokines (IL-6 and IL-8) in human bronchial epithelia cells (NL20), and this effect displays further enhancement after the integration of chitosan and β-cyclodextrin.

Received 21st March 2024
Accepted 13th May 2024

DOI: 10.1039/d4ra02144d

rsc.li/rsc-advances

1. Introduction

Inflammation represents an organism's primary physiological response to multiple diseases, infections, and injuries to tissues.[1,2] Such complicated physiological responses could cause greater damage than normal detrimental stimuli, making medications vital in these situations.[3,4] Patients with cystic fibrosis can face many serious lung disorders due to the inflammatory consequences of chronic bacteria-related infections.[5,6] This frequently leads to the deterioration of pulmonary tissue, reactivation of neutrophils, and chemotaxis. Various antibiotics and anti-inflammatory medications such as azithromycin, ibuprofen, and levofloxacin have been administered to successfully minimize chronic infection-associated inflammation.[6,7] Unfortunately, numerous types of commonly used medications have negative side effects, including disrupted renal function, liver damage, and platelet suppression, in addition to the documented negative impacts on blood pressure.[8]

As an anti-dysentery and antibacterial medication, levofloxacin (LVX) serves as an effective form of fluoroquinolone therapy that is widely administered for treating immunodeficiency and pneumonia.[9–11] In addition to its antimicrobial activities, levofloxacin displays remarkable anti-inflammatory characteristics based on its immune-modulating properties that influence the release of cytokines. The impact on

[a]*Biology Department, College of Science, Princess Nourah Bint Abdulrahman University, Riyadh, Saudi Arabia*
[b]*Zoology Department, Faculty of Science, Beni-Suef University, Beni-Suef, Egypt*
[c]*Department of Biology, College of Science, Imam Mohammad Ibn Saud Islamic University (IMSIU), Riyadh 11623, Kingdom of Saudi Arabia*
[d]*Geology Department, Faculty of Science, Beni-Suef University, Beni-Suef, 65211, Egypt. E-mail: Abukhadra89@Science.bsu.edu.eg; Tel: +2001288447189*
[e]*Materials Technologies and Their Applications Lab, Geology Department, Faculty of Science, Beni-Suef University, Beni-Suef City, Egypt*

interleukin-6 and interleukin-8 levels in human epithelial cells decreases with time.[5,7] Nevertheless, it has been recognized that levofloxacin overdosage can lead to detectable toxicity in the neurological system, digestive system, cardiac system, hematological system, and skin.[12] Additional detrimental impacts associated with excessive dosages of this medication involve a decrease in the binding of plasma proteins and an increase in volume distribution (Vd) and medication clearance.[12] Moreover, these antibiotics are weakly metabolized in the human body, are frequently excreted, and thus enter the natural environment and water bodies as potentially hazardous contaminants.[13,14] Furthermore, the intrusion of remaining medication throughout the environment enhances the evolution of antibiotic-resistant strains of pathogenic bacteria.[7,15] Consequently, several methods were used to regulate the administered drug doses, attain improved therapeutic efficacy, and minimize the undesirable consequences of these types of medications.[16,17] This improvement was suggested to be performed by either providing innovative versions of therapies or improving the efficacy and biological safety of the currently existing traditional types.[18]

There are several effective methods that have been applied to avoid the reported drawbacks, including managed medication delivery, gradual delivery, specific administration, and vigorous pursuit.[2,5] The recently recommended innovative methods of drug administration have a key function in regulating the medication's release level, maintaining the dosage within the required range, promoting site specificity, and maximizing patient compliance.[17,19] Various structures such as clay minerals (montmorillonite and halloysite), zeolites, polymers (chitosan and cellulose), layered double hydroxides (LDHs), hydroxyapatites, and other biomaterials were examined and assessed for this objective.[20–22] The drug's permeability as well as retention quality was significantly improved by previously developed formulations.[23,24] Hydroxyapatite (HAP) is a known biomedical material classified as apatite with a chemical formula of $Ca_{10}(PO_4)_6(OH)_2$. Moreover, it is extensively utilized in multiple medical industries, particularly in the disciplines of bone engineering and drug delivery. Its significant adsorption prospective, ion-exchanging qualities, extended shelf life, broad surface area, flexible framework, and capacity to respond to acidic and basic environments have all been pointed out as reasons for its wide applications.[25–27] It has bioactive, biodegradable, biocompatible, and osteoconductive functions as a biomedical compound without causing inflammation or toxicity. However, its composition's hydrophilic quality reduces its potency as a vehicle for traditional drugs possessing an organic chemical structure.[25,28] Moreover, HAP nanostructures lack stability in acidic environments such as the stomach, rendering them inappropriate for oral delivery.

Consequently, several investigations were performed to improve the shape, chemical structure, and crystallographic sizes of HAP in order to improve its chemical, biological, and physical characteristics. Moreover, this is accomplished *via* modification of its outer surface employing polymer molecules as well as other reacting chemicals.[25] Composite materials consisting of hydroxyapatite (HAP) and synthesized or naturally occurring reactive polymers may help overcome the obstacles hampering the application of HAP in drug administration. The drawbacks include insufficient encapsulation capacity, unregulated release rate, raised fragility, strong tendencies for aggregation, and poor plasticity.[29,30] Furthermore, HAP nanostructures functionalized using carboxyl groups possess better inhibition activities against tumor cell growth than the original particles. Additionally, the composite material may efficiently regulate the release of medications by the carboxyl groups of polymers, improving the binding efficiency of the dissolved medication and the outer surface of HAP particles.[31]

Chitosan, a well-known biopolymer material, is essentially used in pharmacological, environmental, and medicinal industries; it is additionally effective as a carrier for medications.[32–34] It is a polyaminosaccharide compound derived from the chitin constituent that comes from numerous biogenic resources.[32] Chitosan possesses notable hemostatic proficiency, bioactivity, antibacterial potential, safety, biocompatibility, and biodegradable properties, along with favorable mechanical and adsorption characteristics.[34] β-Cyclodextrin (β-CD) is a prominent biopolymer that has already been deeply studied and employed in various hybrid materials including inorganic constituents for a range of industrial activities.[35,36] This is mainly due to its remarkable accessibility, exceptional biocompatibility, notable chemical stability, safe nature, and considerable adsorption properties.[37,38] β-CD is composed of a cyclic glucopyranose framework with six to seven glucose units connected by various (1 → 4) glycosidic linkages. The outermost portion of the structural units is polar, whereas their interiors are hydrophobic.[34] This significantly promotes its integration into hybrids with inorganic constituents and enhances the capacities of synthesized carriers to hold medication molecules.[37,39] β-CD significantly enhances many physicochemical properties of the medication when employed as an administration system, particularly physical stability, therapeutic efficiency, solubility, and chemical reactivity.[40]

Thus, the objective of the present investigation is to analyze the implications of the superficial modifications of magnesium-enriched hydroxyapatite (Mg·HP) using chitosan (CH/Mg·HP) and β-cyclodextrin (CD/Mg·HP) on the characteristics of the resulting bio-composites as effective carriers for levofloxacin. The composites' prospective as carriers was evaluated *via* an in-depth assessment of their loading characteristics and regulating mechanisms, as well as their release aspects and corresponding releasing kinetics. Furthermore, the cytotoxicity characteristics of the assessed structures and their anti-inflammatory qualities following their loading with LVX in response to the generation of cytokines inside the human bronchial epithelia cells were addressed.

2. Experimental work

2.1. Materials

Phosphorite rocks were derived locally from the Qoseir area along the Red Sea in Egypt. It contains P_2O_5 (28 wt%), CaO (46 wt%), SiO_2 (12 wt%), Fe_2O_3 (2 wt%), F (2.8 wt%), Na_2O (4 wt%), MgO (0.5 wt%), Al_2O_3 (0.8 wt%), and LOI (7 wt%).

Magnesium nitrate hexahydrate (99% purity) was applied during the modification of the structure with magnesium. The dissolution and precipitation processes involved using 40% pure nitric acid together with ammonium solution (25% NH_3; CAS number: 1336-21-6), both purchased from Sigma-Aldrich in Egypt. Ethanol (95%), β-cyclodextrin (>85%; MW 1153), powdered chitosan (MW 120,000; 85%), and acetic acid (99.8%) of analytical grade were purchased and used in the hybridizing procedures. Levofloxacin antibiotic ($C_{18}H_{20}N_3O_4F$) (LVX) of 98% purity was used in the cytotoxic, loading, and release studies.

2.2. Synthesis of carriers

2.2.1. Synthesis of magnesium-doped hydroxyapatite (Mg·HAP). By using the dissolution–precipitation method described by Okasha *et al.*,[41] Mg·HAP was produced successfully. The phosphorite starting materials were initially ground to obtain fractions with a size ranging from 25 to 150 μm. Following this, the resulting fractions (15 g) were completely dissolved in HNO_3 (200 mL; 1 M) using a magnetic stirrer for 24 h at a temperature of 343 K. Silicate minerals were removed by filtration, leading to the retention of a solution consisting mainly of Ca^{2+} and PO_4^{3-} as soluble ions. During the subsequent two hours of stirring, the Mg precursor (10 g) was mixed and dissolved effectively in the filtrate. After that, the resulting mixture was progressively mixed with the NH_4OH solution until the effective formation of a white-colored precipitate comprising the obtained HAP phase. Following a day of keeping the synthesis equipment at ambient temperature, the Mg/HAP fractions were obtained *via* an additional filtration step. The produced Mg·HAP particles were subsequently subjected to five runs of washing steps and dried in a muffled oven for a period of ten hours at 373 K.

2.2.2. Synthesis of chitosan/Mg·HAP (CH/Mg·HP) composites. After producing Mg·HAP, a homogeneous mixture of its particles was prepared by dispersing 2 g of the produced HAP in 50 mL of distilled water and treating the resulting suspension with ultrasound waves at 240 W for 120 minutes. Then, 4 g of powdered chitosan was dissolved in 50 mL of diluted (0.1%) acetic acid, and then the obtained solution was added cautiously to the Mg·HAP suspension. The compounds have been blended using a magnetic stirring device at 800 rpm for 24 hours, besides being subjected to ultrasonic waves at a 240 W intensity. The mix was washed thoroughly, filtered to remove any leftover acid, and subsequently dried in an oven at 60 °C for 12 hours. It was later identified as CH/Mg·HAP.

2.2.3. Synthesis of β-cyclodextrin/Mg·HAP (CD/Mg·HP) composites. The Mg·HAP particulates were functionalized with β-cyclodextrin following the procedure described by.[42] The β-cyclodextrin powdered fractions (1 g) were stirred in approximately 80 mL of ethanol using a magnetic stirrer (1000 rpm) over 3 hours till a slurry-like mixture developed. The synthesized Mg·HAP particulates (2 g) were pulverized in 100 mL of distilled water *via* stirring at 1000 rpm with the assistance of a 240 W ultrasound generator for 60 minutes. The Mg·HAP and β-cyclodextrin slurries were blended and homogenized by stirring at 1000 rpm over 24 hours. After that, a further homogenizing stage was performed for 24 hours using an ultrasound generator with a power of 240 W. The hybrid particulates generated were separated from the residual solution using Whatman filter paper with a pore size of 40 μm. The resulting compound was washed with distilled water to neutralize the exterior of the developed CD/Mg·HAP composite and then dried at 60 °C for 12 hours for use in further testing processes.

2.3. Analytical techniques

Depending on the obtained XRD patterns, the level of crystallization and the prevailing crystalline phases were determined using a PANalytical-Empyrean X-ray diffractometer across a measurement range of 0 to 70°. The key functional chemical groups of Mg·HAP, CH/Mg·HAP, and CD/Mg·HAP were identified using a Fourier transform infrared spectrometer (FTIR8400S; Shimadzu) in the frequency range of 400 cm^{-1} to 4000 cm^{-1}. SEM images were acquired using a scanning electron microscope (Gemini, Zeiss Ultra 55) subsequent to applying thin gold coatings over Mg·HAP, CH/Mg·HAP, and CD/Mg·HAP. The assumed transformations in the morphological characteristics of Mg·HAP following the two distinct modifying procedures were successfully assessed with the SEM images retrieved. The surface area and porosity of Mg·HAP, CH/Mg·HAP, and CD/Mg·HAP were measured using a Beckman Coulter SA3100 surface area analyzer considering the resulting N_2 adsorption and desorption isotherm curves.

2.4. LVX loading studies

The LVX encapsulation within Mg·HAP, CH/Mg·HAP, and CD/Mg·HAP was evaluated with respect to the most key variables that can control the embedded LVX dosage and its highest loaded quantities. The investigation assessed the pH range of 3–10, encapsulating time frame of 1 to 22 hours, and LVX content between 100 and 700 mg L^{-1} as the key factors. The Mg·HAP, CH/Mg·HAP, and CD/Mg·HAP particulates were thoroughly mixed with the LVX water-based solutions (50 mL) using a vortex rotator. After each test's equilibrium period, the Mg·HAP, CH/Mg·HAP, and CD/Mg·HAP particulates were separated from the LVX solutions through filtration using Whatman filter paper. The levels of the remaining LVX were measured using an HPLC system (Merck/Hitachi). The residual LVX levels were used to calculate the loading capacities of Mg·HAP, CH/Mg·HAP, and CD/Mg·HAP in mg g^{-1} according to eqn (1). The loading tests of LVX into Mg·HAP, CH/Mg·HAP, and CD/Mg·HAP were performed three times, and the mean values with a standard deviation less than 2.2% were used in the investigated results.

$$\text{Loaded drug } \left(\text{mg g}^{-1}\right) = \frac{(\text{initial concentration} - \text{residual concentration}) \times \text{solvent volume}}{\text{carrier weight}} \quad (1)$$

2.5. Release studies

Using buffering fluids (pH 7.4) at 37.5 °C, the LVX release behaviors of Mg·HAP, CH/Mg·HAP, and CD/Mg·HAP were examined. The LVX-loaded particulates of Mg·HAP, CH/

Mg·HAP, and CD/Mg·HAP (50 mg; 100 mg g^{-1}) were evenly mixed separately in 500 mL of the releasing buffering fluid being tested. The DISTEK dissolution equipment blended the LVX-loaded Mg·HAP, CH/Mg·HAP, and CD/Mg·HAP particulates with the buffering fluid over 120 hours at a rotating speed of 200 rpm. The samples from both the buffering fluids (5 mL) were collected periodically from the bulk volumes of the releasing fluid, and an HPLC system (Merck/Hitachi) was used to evaluate them in order to follow the LVX diffusing % out of Mg·HAP, CH/Mg·HAP, and CD/Mg·HAP. The bulk releasing buffer was promptly refilled by adding the periodically taken samples to maintain the volume consistently throughout the whole releasing duration. The LVX releasing tests were conducted three times, and the mean values were computed employing eqn (2), which has a standard deviation of <3.11%:

$$\text{Drug release}(\%) = \frac{\text{the amount of released LVX}}{\text{amount of loaded LVX}} \times 100 \quad (2)$$

2.6. Anti-inflammatory and toxicity

2.6.1. Cell lines and reagents. Human bronchial epithelial cells (NL20) were purchased from ATCC (American Type Culture Collection) and all tests were performed at the Regional Center for Mycology & Biotechnology, Al-Azhar University, Egypt. Ham's F12 media together with 0.1 mM amino acids, 2 mM L-glutamine, 10 ng mL^{-1} EGF, 1 mg mL^{-1} transferrin, 5 mg mL^{-1} insulin, 500 ng mL^{-1} hydrocortisone, and 4% FBS were employed for the preservation of cells.

2.6.2. Influence of the structures on the production of cytokines. NL20 cells were inserted into 24-well cultivation plates for 24 hours and then cultured inside a serum-free growing mixture for an additional 24 hours. Following that, these cells were treated with approximately 10 ng mL^{-1} of TNF-α to induce the generation of pro-inflammatory cytokines, such as IL-6 and IL-8, inside the NL20 layers. After 48 hours of incubation, the cell culture media were collected and cleared. The levels of IL-6 and IL-8 generated were determined using chemiluminescent enzyme-linked immunosorbent assay (ELISA) kits. The physiological effect of LVX-loaded structures on IL-6 and IL-8 release was investigated by injecting the blended materials together with TNF-α into the cell cultivation medium at different doses. The viability of the cells was assessed using a resazurin viability test.

2.6.3. Influence of the LVX-loaded structure on the viability of NL20. The cells were cultured in a new growth medium containing 5% resazurin for further 4 hours after removing the previously used cell media. Following the incorporation of the dye alongside the completion of the incubating time, the fluorescence signals were measured at an excitation wavelength of 544 nm and an emission wavelength of 590 nm. Analyzed discrepancies between the two data were assessed to determine the level of cell viability. The viability results for the untreated cells were identified as 100%.

2.7. Statistical analysis

The tests were repeated thrice, and the results were expressed as mean ± standard deviation (SD) (S.E.M.; $n = 3$). The statistical evaluation's significance was determined by analyzing the findings of variance (ANOVA) and paired examinations, implementing the value of $*p < 0.05$.

3. Results and discussion

3.1. Characterization of the carrier

3.1.1. XRD analysis. The realized pattern of Mg·HAP indicates the effective formation of HAP with 11.8 nm crystallite size. It peaks were observed prominently at 26.28°, 28.63°, 32.29°, 47.10°, 50.29°, and 64.28° (JCPSD 00-001-1008) (Fig. 1A). The noticeable difference between the peaks' positions comparable to the HAP conventional pattern seems to be a consequence of the crystallographic impact of the implemented Mg^{2+} ions.[43,44] The diffraction peaks corresponding to the introduced polymer, which are situated at approximately 10° and 22° angles, reveal that the integrated chitosan displays semi-crystalline properties (Fig. 1B). XRD analysis of the CH/Mg·HAP blend clearly demonstrates the dominant peaks corresponding to the Mg·HAP phase; nevertheless, they slightly shifted towards lower positions (Fig. 1C). One of the principal peaks of CH had to be eliminated, and a second peak was fluctuated and paired with Mg·HAP key peaks, indicating an effective integration between Mg·HAP and CH. The diffraction pattern of β-cyclodextrin as a distinct phase reveals the highly

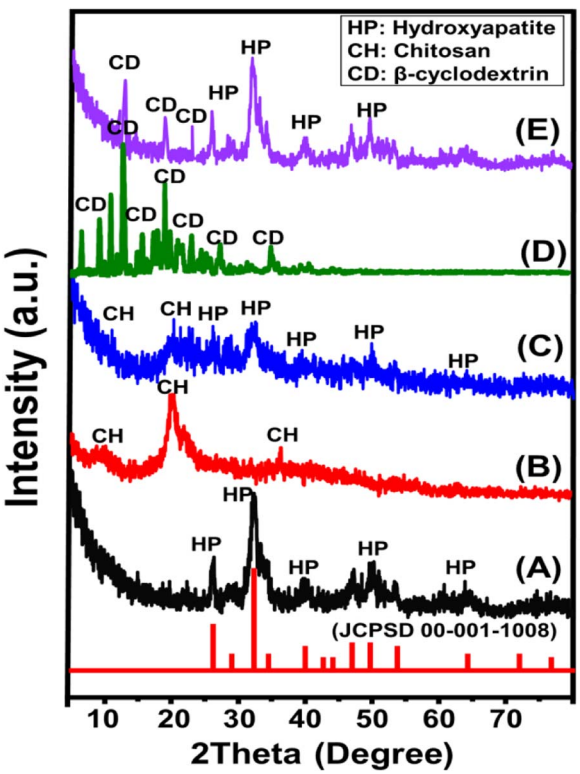

Fig. 1 XRD patterns of Mg·HAP (A), chitosan (B), CH/Mg·HAP (C), β-cyclodextrin (D), and CD/Mg·HAP (E).

crystalline structure of the polymeric precursors implemented, displaying multiple strong peaks at specific 2 Theta angles ranging from 6.80° to 34.90° (Fig. 1D). The CD/Mg·HAP pattern contains common peaks of Mg·HAP and embedded β-cyclodextrin; however, they are situated at significantly distinct positions (Fig. 1E). This pattern indicates that Mg·HAP has hybridized and functionalized with β-cyclodextrin, probably involving hydrogen bonds and chemical complexes in addition to the expected grafting of β-CD onto the structure of Mg·HAP.

3.1.2. SEM analysis. The produced Mg·HAP is composed of needle-shaped nanoparticles that are interconnected, developing branched frameworks or bundle-like aggregated morphologies (Fig. 2A). The irregular arrangement of bundles alongside the manner in which they crossed each other formed a porous framework together with the crystalline pores that already existed within the framework of HAP (Fig. 2B). The Mg-HAP-bundled particles are highly ornamented with nano-exposed burrs. The Mg·HAP-forming bundles had an average diameter between 20 and 60 nm and an average length between 50 and 250 nm. The filamentous nanoparticles inside each bundle exhibited a mean diameter that fluctuated between 2 and 10 nm and a mean length that varied between 20 and more than 100 nm. The SEM images of the produced particles comprising the CH/Mg·HAP composite revealed significant blending between the CH polymeric structure and Mg·HAP particles (Fig. 2C and D). The Mg·HAP grains significantly underwent reorientation and rearrangement as aggregated particles (Fig. 2C and D). This resulted in an irregular exterior composed of intersecting particulates with varying geometries and including a number of interstitial cavities as secondary nano-pores (Fig. 2D).

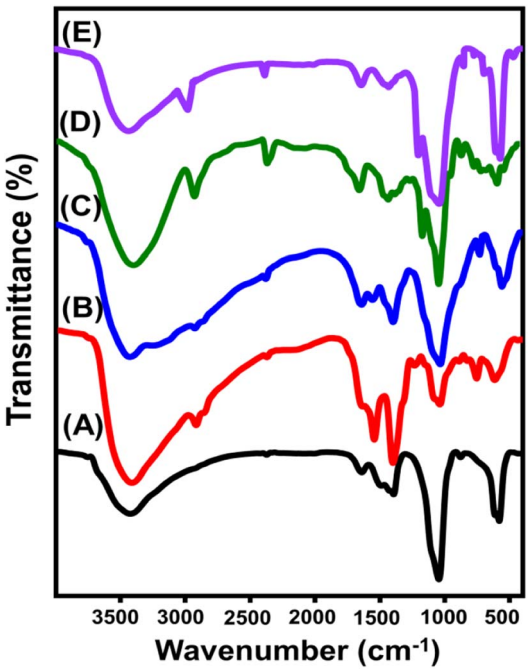

Fig. 3 FT-IR spectra of Mg·HAP (A), chitosan (B), CH/Mg·HAP (C), β-cyclodextrin (D), and CD/Mg·HAP (E).

The SEM photographs of the produced CD/Mg·HAP reveal a significant alignment and entrapment of the HAP crystals through the blocky frameworks of β-CD. This leads to the formation of aggregates that have various morphologies (Fig. 2E and F). The Mg·HAP particles are arranged randomly throughout the polymer, yielding an uneven and rough surface

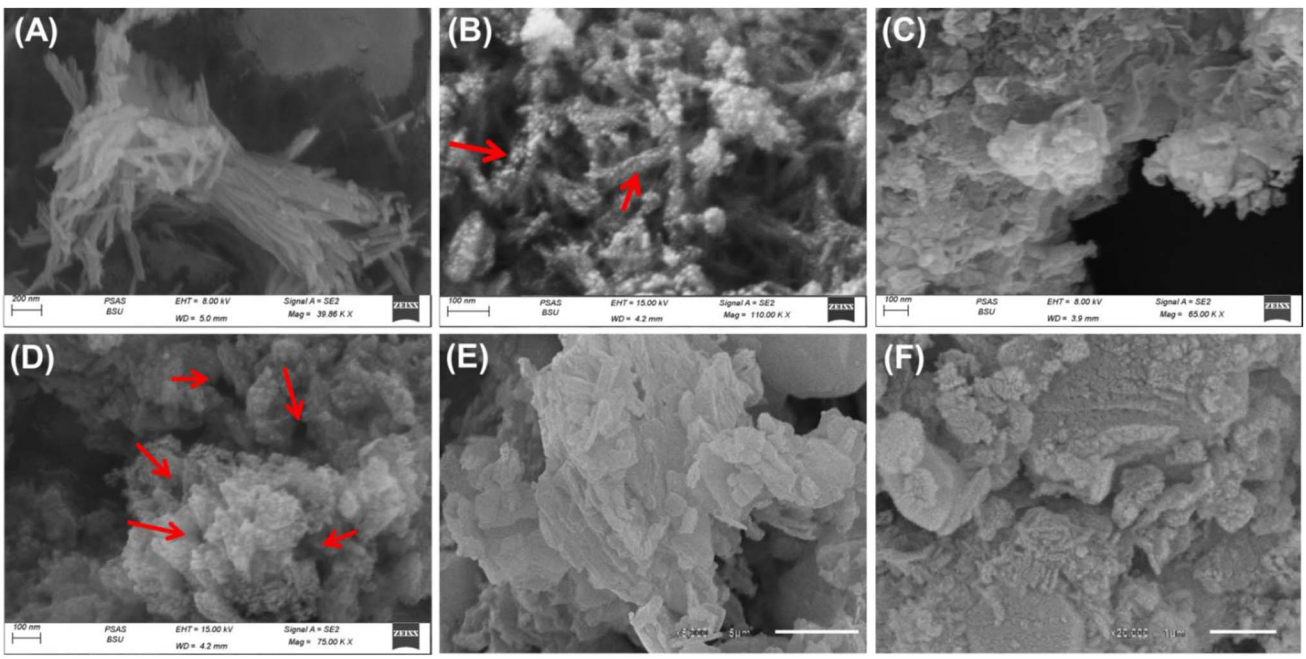

Fig. 2 SEM images showing the geometry and surface of Mg·HAP (A and B), prepared CH/Mg·HAP composite (C and D), and prepared CD/Mg·HAP composite (E and F).

that may increase the surface area and interface exposures. A substantial interaction between both β-CD and Mg·HAP resulted in the development of an interconnected structure comprising curved platelets or lenticular-like particles. The morphological modifications are associated with considerable changes in textural characteristics, particularly surface area. The original surface area of Mg.HPA (93.7 $m^2\ g^{-1}$) increased dramatically to 101.3 $m^2\ g^{-1}$ and 95.2 $m^2\ g^{-1}$ after including CH (CH/Mg·HAP) and β-CD (CD/Mg·HAP), respectively.

3.1.3. FT-IR analysis. The FT-IR spectra of the synthesized hybrids, together with the mixed constituents, were investigated to detect the variations in the chemical compositions across the modification procedures (Fig. 3). The fundamental components of HAP were easily recognized through the spectrum results for Mg·HPA. The analysis confirmed the existence of O–H (3434.4 cm^{-1}) and important phosphorus-containing groups, particularly asymmetrical P–O of PO_4^{3-} (1039 cm^{-1}) and HPO_4^{2-} (871 cm^{-1}), as well as symmetrical O–P–O (570 cm^{-1}) and asymmetrical O–P–O (603 cm^{-1}) corresponding to PO_4^{3-} (Fig. 3A).[25,44–46] The spectral bands corresponding to chitosan that was incorporated inside the CH/Mg·HP blend displayed their prevalent bands, representing N–H (1547 cm^{-1}), C–O (1040 cm^{-1}), C–H (2925 and 1336 cm^{-1}), C=O (1637 cm^{-1}), and C–N (1402 cm^{-1})[32,33] (Fig. 3B). The CH/Mg·HAP spectral patterns show notable variations in positions and intensities after a successful integrating process, revealing complex bands that correspond to organic chitosan as well as inorganic HAP (Fig. 3C). Chitosan possesses distinct functional groups including C=O (1640 cm^{-1}), C–H (2925 cm^{-1}), and C–N (1397 cm^{-1}). The HAP could be distinguished by its distinctive groups: PO_4^{3-} at about 1034 and 559 cm^{-1} and CO_3^{2-} at roughly 2379 cm^{-1} (Fig. 3C). The shifts in the positions and intensities of the FT-IR bands, together with the reduction in the spectrum of some important groups such as HPO_4^{2-} in Mg·HAP and N–H in chitosan, validate the significant interaction involving these chemical groups during the composite's formation.

The β-CD spectra revealed the corresponding bands of its structure as distinctive phases around 3376 cm^{-1} (O–H), 2926 cm^{-1} (asymmetric CH/CH_2 bonding), 1666 cm^{-1} (H–O–H deformation), 1482 cm^{-1} (hyperfine C=H), 1000 cm^{-1} (C–O), 1158 cm^{-1} (glycosidic C–O–C), and 1200 cm^{-1} (C–O–C stretching) (Fig. 3D).[38,39] The CD/Mg·HAP spectrum demonstrates the existence of characteristic bands corresponding to the chemical constituents of Mg·HAP, involving OH at 3424 cm^{-1} and P–O at 1040 and 571 cm^{-1}, alongside the corresponding bands of β-CD including C=H around 2905 cm^{-1}, hyperfine C=H around 1468 cm^{-1}, C=C around 1663 cm^{-1}, and C–O–C around 1211 cm^{-1} (Fig. 3E). The successful production of the CD/Mg·HAP blended material is supported by its formation of such intricate organic and inorganic chemical bonds, along with major shifts in the positions of identification bands. The results confirm the substantial chemical interaction between both of these constituents.

3.2. Encapsulation of the LVX drug

3.2.1. Influence of the encapsulation parameters

3.2.1.1. Effect of pH. Keeping the rest of the factors fixed, the effects of various pH levels (from 3 to 9) on the loading properties were investigated [dose: 20 mg; LVX levels: 100 mg L^{-1}; temperature: 20 °C; duration: 2 h]. It was established that increased pH levels significantly improve LVX's encapsulating properties (Fig. 4A). This could be detected between pH 3 (Mg·HAP (25.8 mg g^{-1}), CH/Mg·HAP (30.5 mg g^{-1}), and CD/Mg·HAP (32.7 mg g^{-1})) and pH 8 (Mg·HAP (87.6 mg g^{-1}), CH/Mg·HAP (98.5 mg g^{-1}), and CD/Mg·HAP (105.3 mg g^{-1})). At pH levels above 8, the three vehicles exhibited a noticeable decrease in their ability to accommodate additional soluble LVX molecules, which displayed a reversal impact under highly alkaline conditions (Fig. 4A). This behavior can potentially be interpreted by considering the ionizing features of the LVX molecules alongside the exterior charges of the particles investigated as carriers. LVX in its soluble form was detected as a cationic type exhibiting a positive charge through pH levels below 5. These species were generated through the protonation reaction of the piperazinyl groups.[20] The zwitterionic type of LVX was detected between pH 5 and pH 8.5.[5,47] At pH levels higher than 8.5, the LVX molecules were determined to exist as anions due to the predicted de-protonation characteristics of their carboxyl groups.[48,49] Acidic conditions do not seem favorable for the loading of LVX in its cationic state. It will encounter electrostatic repellent forces against the positive-charged functional groups of the particles of the carriers impacted by protonation reactions under acidic conditions.[50] The deprotonated sites that exist throughout the surfaces of the carriers in alkaline solutions (pH > 8) repel soluble LVX ions that exist in the anionic types under these conditions.[20] Consequently, it was suggested that the loading pH should be adjusted between pH 7 and close to pH 8 to be able to accomplish the most effective loading for LVX medication.

3.2.1.2. Loading duration. The influence of the duration on the Mg·HAP, CH/Mg·HAP, and CD/Mg·HAP loading performances was explored experimentally throughout a time frame of 1–22 hours while maintaining all the remaining variables constant [pH: 8; volume: 50 mL; LVX level: 200 mg L^{-1}; temperature: 20 °C; dose: 20 mg]. Throughout the course of the study duration, there was an obvious enhancement in the LVX loading efficiencies by Mg·HAP, CH/Mg·HAP, and CD/Mg·HAP in regard to the loading speeds and loaded amounts in mg g^{-1} (Fig. 4B). The enhancement is noticeable between 1 and 6 hours for Mg·HAP and up to 10 hours for CH/Mg·HAP and CD/Mg·HAP. After these periods, further increasing the time frame of testing has very little or no impact on the rate of loading or the quantity of LVX loaded. The graphs demonstrate stable behaviors with consistent results above these time frames (Fig. 4B). These qualities display the equilibrium situations of the HAP-based drivers of LVX, as well as corresponding equilibrium capacities (137.6 mg g^{-1} (Mg·HAP), 189.7 mg g^{-1} (CH/Mg·HAP), and 221.8 mg g^{-1} (CD/Mg·HAP) (Fig. 4B). The presence of substantial quantities of functioning binding sites in the free forms throughout the beginning of the encapsulating operations could potentially be responsible for the noticed significant loading rates along with a rapid rise in the LVX-

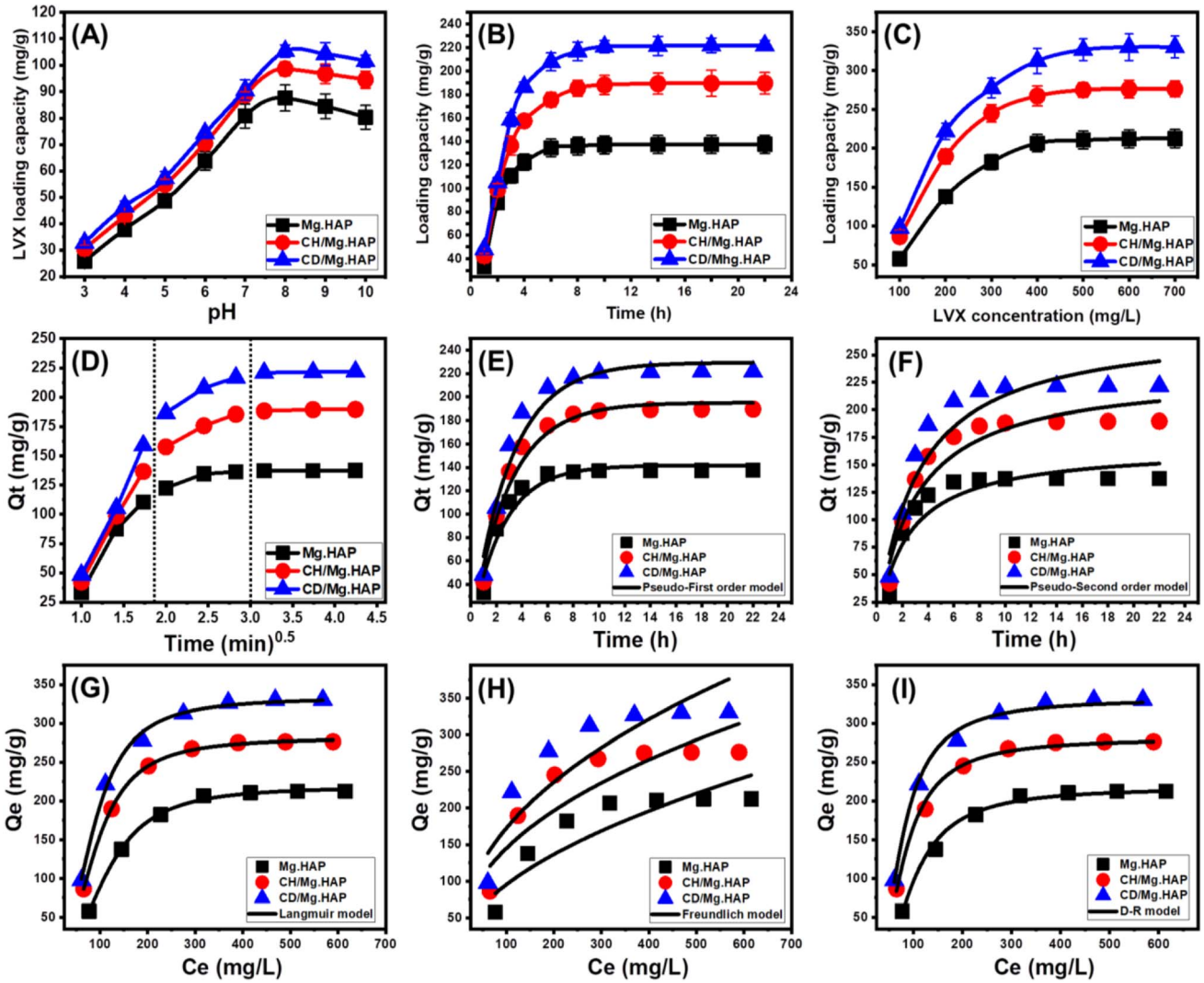

Fig. 4 Impact of the solution pH on LVX loading performances (A), influence of loading time frame (B), impact of the starting LVX content (C), intra-particle diffusion curves for LVX loading reactions (D), kinetic modeling behaviors of LVX loading process (E and F), and traditional isotherm modeling of LVX loading process (G (Mg·HAP), H (CH/Mg·HAP), and I (CD/Mg·HAP)) (the tests were performed thrice, and the results are expressed as mean values with a standard deviation of 2.2%).

loaded amounts.[51] The quantity and accessibility of the unoccupied sites throughout Mg·HAP, CH/Mg·HAP, and CD/Mg·HAP are dramatically decreased as a result of the continuous occupation of them by LVX during the course of the examinations. Therefore, as time progressed, the measurable encapsulation rate of LVX dropped drastically by the end of the period under investigation. Moreover, the loading characteristics of LVX into the HAP-based carriers did not show notable improvements. When all of the positions were filled with LVX molecules, their loading equilibrium conditions were obtained.[52]

3.2.1.3. LVX concentration. Various levels of LVX were examined to determine their impact on the loading qualities of HAP-based carriers. The LVX contents ranged from 100 to 700 mg L^{-1}, while additional variables such as duration (22 h), temperature (20 °C), dosage (20 mg), pH (8), and volume (50 mL) were maintained. The maximum performances and equilibrium behaviors of Mg·HAP, CH/Mg·HAP, and CD/Mg·HAP mostly rely on the initially applied content of LVX. At elevated starting levels of LVX, the entire amount of embedded LVX within Mg·HAP, CH/Mg·HAP, and CD/Mg·HAP increased dramatically (Fig. 4C). The LVX ions' driving forces and migration characteristics were greatly enhanced, as they were present at a notably high level within a certain volume. This enhances the potential of collision and facilitates the chemical contact that exists among the binding sites of HAP-based carriers and the drug's water-soluble ions.[34,53] Subsequently, this enhances the LVX loading performance till definite levels (400 mg L^{-1} for Mg·HAP and 500 mg L^{-1} for CH/Mg·HAP and CD/Mg·HAP) (Fig. 4C). When the LVX levels exceed a certain point, any further increase in the evaluated LVX content does not affect the detectable loaded amounts of medication, which typically represent the corresponding equilibrium phases of Mg·HAP, CH/Mg·HAP, and CD/Mg·HAP (Fig. 4C). Therefore, Mg·HAP,

CH/Mg·HAP, and CD/Mg·HAP (212.6 mg g^{-1} for Mg·HAP, 276.4 mg g^{-1} for CH/Mg·HAP, and 330.4 mg g^{-1} for CD/Mg·HAP) complete their highest possible loading capacities. The higher LVX encapsulating effectiveness of CH/Mg·HAP and CD/Mg·HAP *versus* Mg·HAP might be a consequence of some factors involving the increased surface area post-modification, the organophilic qualities of CH/Mg·HAP and CD/Mg·HAP, which enhance their attraction to LVX, and the extra binding sites following the hybridization.

3.2.2. Loading mechanism

3.2.2.1. Kinetic properties

3.2.2.1.1. Intra-particle diffusion behavior. Three distinctive stages, lacking any crossovers with the curves' beginning points, can be detected within the intra-particle diffusion curves comprising the encapsulating reactions of LVX inside Mg·HAP, CH/Mg·HAP, and CD/Mg·HAP (Fig. 4D). This demonstrates the cooperative mechanisms that are responsible for the loading of LVX in addition to the substantial impact of the medication ions' diffusion pathways closer to the binding interfaces of Mg·HAP, CD/Mg·HAP, and CH/Mg·HAP.[53,54] This could involve adsorption onto reactive receptors across the external surface, layered adsorption, intra-particle diffusion, and the implications of saturated or equilibrium status.[55] The initial phase indicates the operation of exterior loading processes during the early stages of the testing, while the number of surficial-reacting receptors found controls the progression of the encapsulating outcomes (Fig. 4D).[56] An additional phase was noticed by prolonging the duration. This phase indicates the involvement of several regulating pathways such as the influence of layered loading actions by interior receptors and LVX diffusion behaviors. The third step was recognized as the predominant portion that was associated with the LVX encapsulating equilibrium situations of Mg·HAP, CH/Mg·HAP, and CD/Mg·HAP (Fig. 4D). This confirms the occupation or use of all the functional binding positions by the LVX ions introduced.[25,53] The loading reactions that occur in this stage are regulated by many pathways involving molecular and/or interionic attractions.[34]

3.2.2.1.2. Kinetic modeling. The kinetic characteristics of the LVX encapsulating processes into HAP-based carriers are described based on the fundamental hypotheses of pseudo-first order (P.F.) (eqn (3)) and pseudo-second order (P.S.) (eqn (4)). The presented symbols of the equations including Q_t (mg g^{-1}), K_1 (1/min), Q_e (mg g^{-1}), and K_2 (g mg^{-1} min^{-1}) denote the quantity of loaded molecules at time t, rate constant of P.F. model, equilibrium loading capacity, and rate constant of P.S. model, respectively. The consistency that exists between the loading activities and kinetic theories of these two models was examined through non-linear fitting, employing their describing formulas. The correlation coefficient (R^2) and chi-squared (χ^2) values were used as indicators of the model-fitting accuracy (Table 1; Fig. 4E and F).

$$Q_t = Q_e\,(1 - e^{-k_1 \cdot t}) \quad (3)$$

$$Q_t = \frac{{Q_e}^2 k_2 t}{1 + Q_e k_2 t} \quad (4)$$

The calculated R^2 and χ^2 results imply that the kinetic aspects of the P.F. model better describe the LVX encapsulating activities within the three tested carriers, comparable to the P.S. theory. The actual equilibrium capacities (137.6 mg g^{-1} (Mg·HAP), 189.7 mg g^{-1} (CH/Mg·HAP), and 221.8 mg g^{-1} (CD/Mg·HAP)) closely matched the mathematically predicted values derived by the P.F. simulation (141.6 mg g^{-1} (Mg·HAP), 195.1 mg g^{-1} (CH/Mg·HAP), and 229.5 mg g^{-1} (CD/Mg·HAP), confirming the precision of the fitting findings. The immobilization of LVX inside these structures was mainly induced by physical mechanisms such as van der Waals forces and electrostatic forces, depending on the kinetic aspects of the P.F. model.[57,58] Nevertheless, the P.F. theory more accurately describes the loading activities *versus* the P.S. hypothesis; the fitting results are still considerably compatible with the P.S. theory. It was assumed that particular chemical processes such as electron sharing, hydrogen bonding, and hydrophobic bonding had a minor impact or provided some assistance throughout the processes of loading LVX inside Mg·HAP, CH/Mg·HAP, and CD/Mg·HAP.[53,57] The interaction of chemical and physical interactions resulted in the development of a layer of the loaded drug by chemical activities, which was then used as a base for the formation of another loaded layer involving physical activities.[59]

3.2.2.2. Isotherm properties

3.2.2.2.1. Classic isotherm models. The equilibrium characteristics of loading LVX onto the different HAP forms as prospective carriers were analyzed using the Langmuir (eqn (5)) and Freundlich (eqn (6)) models, together with the Dubinin-Radushkevich (D-R) (eqn (7)) criteria. The declared symbols in the equations such as Q_e (mg g^{-1}), Q_{max} (mg g^{-1}), C_o (mg L^{-1}), C_e (mg L^{-1}), b (L mg^{-1}), K_f (mg g^{-1}), Q_m (mg g^{-1}), β (mol^2 kJ^{-2}), and ε (kJ^2 mol^{-2}) refer to equilibrium loading capacity, expected maximum capacity, initial drug concentration, rest concentration, Langmuir constant, Freundlich constant, loading capacity, D-R constant, and Polanyi potential, respectively. The results were non-linearly fitted using the described formulas of the models, and the level of match was established according to the correlation coefficient (R^2) alongside chi-squared (χ^2) values (Table 1; Fig. 4G–I).

$$Q_e = \frac{Q_{max} b C_e}{(1 + b C_e)} \quad (5)$$

$$Q_e = K_f {C_e}^{1/n} \quad (6)$$

$$Q_e = Q_m e^{-\beta \varepsilon^2} \quad (7)$$

Based on the given model-fitting factors, it can be concluded that the insertion of LVX into the different forms of HAP exhibits Langmuir isotherm qualities instead of the Freundlich proposed theory. As a result, LVX ions were evenly entrapped onto the exteriors of them, forming monolayer layers, by several regularly and consistently dispersed reactive receptors.[25,56] The favored sequestration of LVX molecules within Mg·HAP, CH/Mg·HAP, and CD/Mg·HAP vehicles can be detected according to the computed values of RL parameter <1.0. The maximal hypothesized loading levels of LVX within Mg·HAP, CH/

Table 1 Determined theoretical variables for loading kinetics, equilibrium, and release kinetic models under study

Model	Parameters	Mg·HAP	CH/Mg·HAP	CD/Mg·HAP
Kinetic models				
Pseudo-first-order	K_1 (min^{-1})	0.40	0.34	0.32
	$Q_{e\ (Cal)}$ (mg g^{-1})	141.6	195.1	229.5
	R^2	0.95	0.97	0.97
	X^2	1.11	0.91	1.24
Pseudo-second-order	k_2 (g mg^{-1} min^{-1})	0.00258	0.00148	0.0018
	$Q_{e\ (Cal)}$ (mg g^{-1})	167.1	235.0	278.2
	R^2	0.90	0.93	0.92
	X^2	2.34	2.27	2.94
Isotherm models				
Langmuir	$Q_{max\ (mg\ g^{-1})}$	218.6	281.5	333.2
	b (L mg^{-1})	7.41×10^{-6}	1.69×10^{-5}	2.15×10^{-5}
	R^2	0.99	0.99	0.99
	X^2	0.04	0.01	0.188
	RL	0.99	0.98	0.98
Freundlich	$1/n$	0.52	0.44	0.45
	k_F (mg g^{-1})	8.7	19.3	21.8
	R^2	0.85	0.83	0.84
	X^2	6.6	7.8	9.1
D-R model	β (mol^2 kJ^{-2})	0.01052	0.00772	0.00662
	Q_m (mg g^{-1})	217.4	280.6	331.5
	R^2	0.99	0.99	0.99
	X^2	0.22	0.15	0.21
	E (kJ mol^{-1})	6.89	8.04	8.7
Monolayer model of one energy	n	2.48	2.43	2.40
	N_m (mg g^{-1})	88.03	115.8	138.5
	$Q_{(sat)}$ (mg g^{-1})	218.3	281.4	332.4
	ΔE (kJ mol^{-1})	−4.69	−4.11	−3.98

Release kinetics	Determination coefficient		
	Mg·HAP	CH/Mg·HAP	CD/Mg·HAP
Zero-order	0.87	0.79	0.83
First-order	0.95	0.91	0.98
Higuchi	0.96	0.94	0.97
Hixson-Crowell	0.93	0.99	0.99
Korsmeyer-Peppas	0.95	0.97	0.96
n	0.74	0.79	0.77

Mg·HAP, and CD/Mg·HAP were computed using the parameters of the Langmuir isotherm and found to be 218.6 mg g^{-1}, 281.5 mg g^{-1}, and 333.2 mg g^{-1}, respectively.

The isothermal characteristics of the studied D-R model could provide insights into the energy variations across the surfaces of the three carriers, independent of their levels of homogeneity or heterogeneity.[60] Calculating the Gaussian energy (E) according to the D-R simulation highlights the key loading mechanisms, whether they are chemically or physically controlled reactions. The physical mechanisms display a Gaussian energy below 8 kJ mol^{-1}, but the chemical activities display levels exceeding 16 kJ mol^{-1}. Gaussian energies ranging from 8 to 16 kJ mol^{-1} indicate the presence of complicated systems or poor chemical processes.[25,60] The Gaussian energies for the loading of LVX within Mg·HAP, CH/Mg·HAP, and CD/Mg·HAP are 6.89 kJ mol^{-1}, 8.04 kJ mol^{-1}, and 8.7 kJ mol^{-1}, respectively (Table 2). The findings indicated a significant influence of the physical mechanisms throughout the uptake of LVX by Mg·HAP along with a potential effect of ion exchange mechanisms (ranging from 0.6 kJ mol^{-1} to 25 kJ mol^{-1}). However, the uptake of these molecules by CH/Mg·HAP and CD/Mg·HAP demonstrate values within the reported limits of co-operated physical and week chemical mechanistic processes involving ion exchange reactions.

3.2.2.2.2. Advanced isotherm models. Following the basic principles of statistical physics hypothesis, the specified improved isotherm models provide more understanding about Mg·HAP, CH/Mg·HAP, and CD/Mg·HAP as LVX vehicles with respect to their surfaces/medication ions interfaces. Using a monolayer model with a single energy (eqn (8)) and its corresponding mathematical factors, including steric in addition

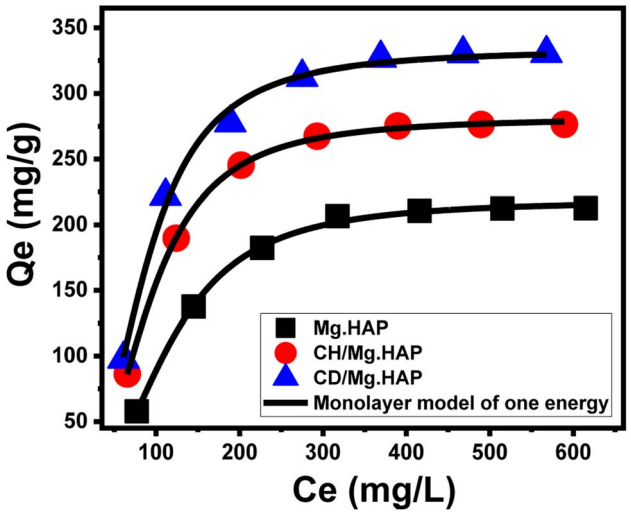

Fig. 5 Fitting of the LVX loading reactions with the monolayer model of one energy site.

to energetic factors, both the loading behaviors and underlying controlled mechanistic processes were investigated (Fig. 5; Table 1). The primary determinants of the fitting levels were the determination coefficients (R^2) and root-mean-square error (RMSE).

$$Q_e = \frac{nN_M}{1 + \left(\frac{C_{1/2}}{C_e}\right)^n} \quad (8)$$

The steric aspects encountered statistically included the existing and effective receptors density ($N_{m\ (LVX)}$) throughout the investigated HAP based carriers, the number of LVX ions that were entrapped into a single effective receptor ($n_{(LVX)}$), and their saturation loading levels ($Q_{sat\ (LVX)}$). The assessed energetic factor represented the LVX loading energy (E). The $N_{m\ (LVX)}$ computed values expanded considerably after the modification of Mg·HAP to form CH/Mg·HAP (115.8 mg g^{-1}) and CD/Mg·HAP (138.5 mg g^{-1}), compared to the initial value of Nm $_{(LVX)}$ = 88.03 mg g^{-1}. The integration of a greater number of active and unbound functional units corresponding to combined chitosan and β-CD might be the reason for this, or it could be a consequence of the enhancement in the interaction interfaces that arise in surface area. Following modifications, the saturation levels of Mg·HAP, CH/Mg·HAP, and CD/Mg·HAP increased drastically from 218.3 mg g^{-1} to 281.4 mg g^{-1} and 332.4 mg g^{-1}, respectively. The total number of filled LVX ions into each reactive receptor throughout Mg·HAP, CH/Mg·HAP, and CD/Mg·HAP ($n_{(LVX)}$) illustrates the substantial influence of the modifying steps on the qualities of Mg·HAP interfaces as a drug vehicle, particularly by β-CD. Based on mathematical calculations, the number of LVX ions entrapped into each single site across Mg·HAP, CH/Mg·HAP, and CD/Mg·HAP is 2.48, 2.43, and 2.4, respectively. The values are greater than 1, indicating the vertical ordering of the loaded ions onto their external surfaces and their encapsulation through multi-molecular processes.[61,62]

The corresponding loading energies (E) were calculated using eqn (9), employing the mathematically determined remaining LVX contents during the half saturation levels ($C_{1/2}$) and their solubility (S) at temperature (T):

$$\Delta E = -RT \ln\left(\frac{S}{C_{1/2}}\right) \quad (9)$$

The calculated binding energies for loading LVX throughout Mg·HAP, CH/Mg·HAP, and CD/Mg·HAP were −4.69 kJ mol^{-1}, −4.11 kJ mol^{-1}, and −3.98 kJ mol^{-1}, respectively. This supports the latest outcomes concerning the physical encapsulating of LVX within the three structures.[62] The processes may include van der Waals forces with an energy change of 4 to 10 kJ mol^{-1}, dipole forces with an energy change of 2 to 29 kJ mol^{-1}, and hydrogen binding with an energy change less than 30 kJ mol^{-1}.[63,64]

3.3. *In vitro* release profiles

The releasing patterns of Mg·HAP, CH/Mg·HAP, and CD/Mg·HAP were evaluated by analyzing the levels of LVX molecules that diffused out. The LVX diffused% out of the tested HAP derivatives through the used releasing buffer shows significant differences in releasing rates with the expanding releasing periods. The release rates of LVX out of Mg·HAP, CH/Mg·HAP, and CD/Mg·HAP exhibit rapid aspects that correspond to noticeable variations in the detected levels of LVX liberated (Fig. 6). Following certain time intervals, the measurable diffusing rates of LVX notably reduced, with no noticeable enhancement in the amounts liberated (Fig. 6). At this point, Mg·HAP, CH/Mg·HAP, and CD/Mg·HAP releasing activities were stabilized. The rapid diffusion of LVX noticed throughout the initial release stages was ascribed to the abrupt desorption of loosely bound and physically trapped LVX ions out of the exterior receptors.[65–67] After the complete liberation of weakly embedded LVX ions from their surfaces, the releasing behavior

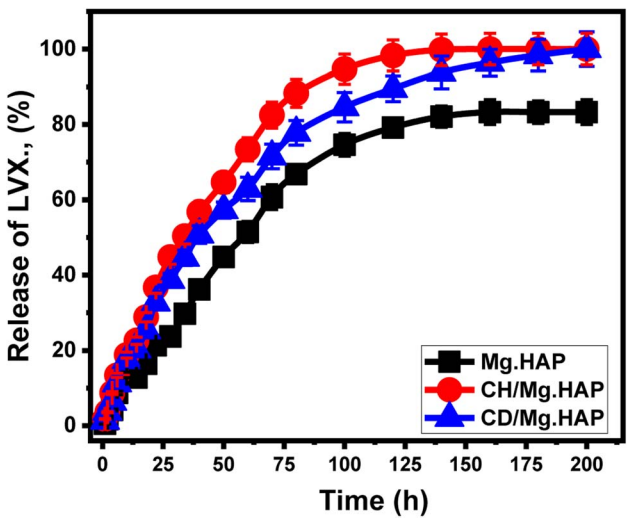

Fig. 6 Release profiles of Mg·HAP, CH/Mg·HAP, and CD/Mg·HAP structures.

was regulated by strongly embedded ions along with the ions that were integrated in chemical complexes, in addition to the encapsulated LVX ions within the internal pores, which hindered the diffusion efficiency.[20,68,69]

The releasing behaviors of LVX from Mg·HAP in gastric and intestinal fluids were consistent for more than 200 hours. Around 50% of the tested LVX dose was liberated out of the Mg·HAP framework after 60 hours. Even after 200 hours, no complete LVX-releasing levels were detected (83.3%) (Fig. 6). The hypothesized powerful hydrogen bonding that exists between the adsorbed LVX ions and the predominant reactive functional components of synthesized hydroxyapatite might clarify the slow release behavior of Mg·HAP.[70] This hinders the release of LVX ions out of the HAP framework, limiting the effective administration of the drug within therapeutic levels. The release behaviors of LVX from CH/Mg·HAP exhibit more rapid features than those of Mg·HAP (Fig. 6). Approximately 50% of the trapped quantity of LVX was released out of the framework of CH/Mg·HAP within 34 hours and the complete release required 160 hours. Hybridizing Mg·HAP with β-CD (CD/Mg·HAP) enhanced the liberation of LVX ions as compared to Mg·HAP but at a slower rate than that of CH/Mg·HAP; 50% of the LVX was liberated out of the CD/Mg·HAP after 40 hours and LVX was entirely released within 200 hours (Fig. 6).

Hybridizing Mg·HAP utilizing chitosan alongside β-cyclodextrin results in an enhancement in the release speed of loaded LVX molecules. These biopolymers provide barriers across the interfaces between the reactive binding groups of Mg·HAP and the adsorbed LVX drug's molecular framework. This blocked the expected hydrogen binding that normally

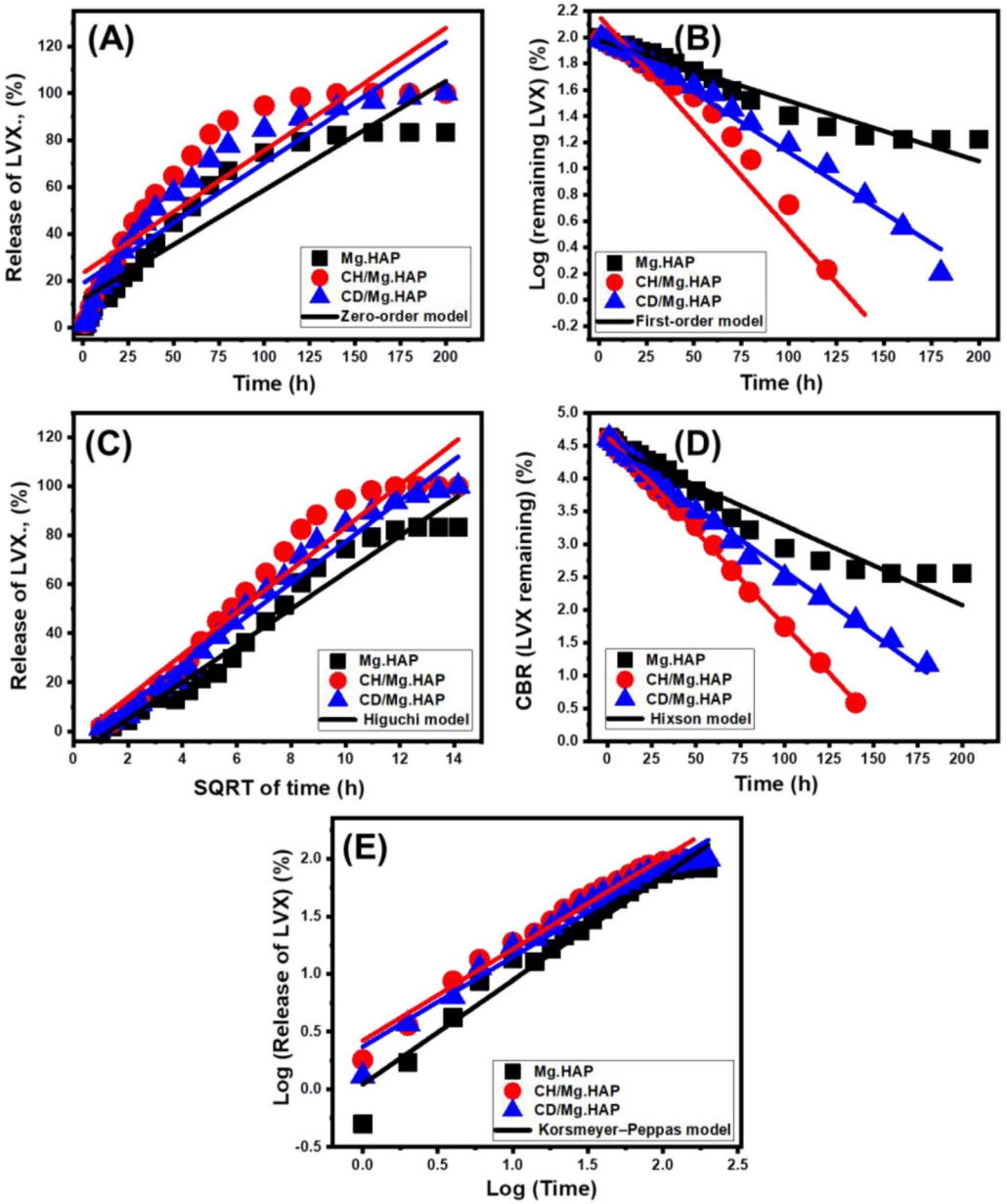

Fig. 7 Fitting of LVX release results with zero-order (A), first-order (B), Higuchi (C), Hixson-Crowell (D), and Korsmeyer-Peppas (E) models.

occurs between the drug's framework and the OH-containing chemical groups of Mg·HAP, leading to fast diffusion of the medication molecules. The uniform distribution of LVX ions throughout the polymeric chain matrix significantly enhances their diffusing characteristics. Moreover, the modification methods add more chemical functionalities, enhancing the potential of LVX to be physically trapped onto such surface sites or receptors. Gradually and cautiously diffusing LVX as a form of chemotherapy is advisable under specific situations when there is a need for extended contact and exposures among the administrated medication and cancerous cells.[20,71] Furthermore, sudden and rapid administration approaches are advised in particular situations when it is necessary to provide exact medicinal dosages within short durations. The synthesized CH/Mg·HAP and CD/Mg·HAP composites might serve as promising carriers for LVX, providing a controlled delivery vehicle with excellent encapsulation and release properties based on the adjusted ratios of the hybridized polymer.

3.4. Release kinetic studies

As indicators of the well-controlled mechanistic processes, kinetic analyses of the LVX releasing activities out of the prepared HAP derivatives were performed. The release operations were modeled using zero-order (Z-O) (eqn (10)), first-order (F-O) (eqn (11)), Higuchi (H-G) (eqn (12)), Hixson-Crowell (H-C) (eqn (13)), and Korsmeyer-Peppas (K-P) (eqn (14)) kinetic theoretical models. The modeling processes were highlighted based on the linear regression fitting levels.[20]

$$W_t - W_0 = K_0 \cdot t \tag{10}$$

$$\ln(W_\infty / W_t) = K_1 \cdot t \tag{11}$$

$$W_t = K_h t^{1/2} \tag{12}$$

$$W_o^{1/3} - W_t^{1/3} = K_{HC} t \tag{13}$$

$$W_t / W_\infty = K_p t^n \tag{14}$$

The zero-order kinetic aspects suggest that the diffusion activities of LVX through Mg·HAP, CH/Mg·HAP, and CD/Mg·HAP carriers proceed at consistent rates, unaffected by the loading dosages.[23] LVX-loaded dosages into them significantly affect the releasing performance according to the F-O assumption. The Higuchi kinetics concept suggests that diffusion phenomena play a key role in releasing processes.[35,72] The diffusion activities following Higuchi kinetics were conducted

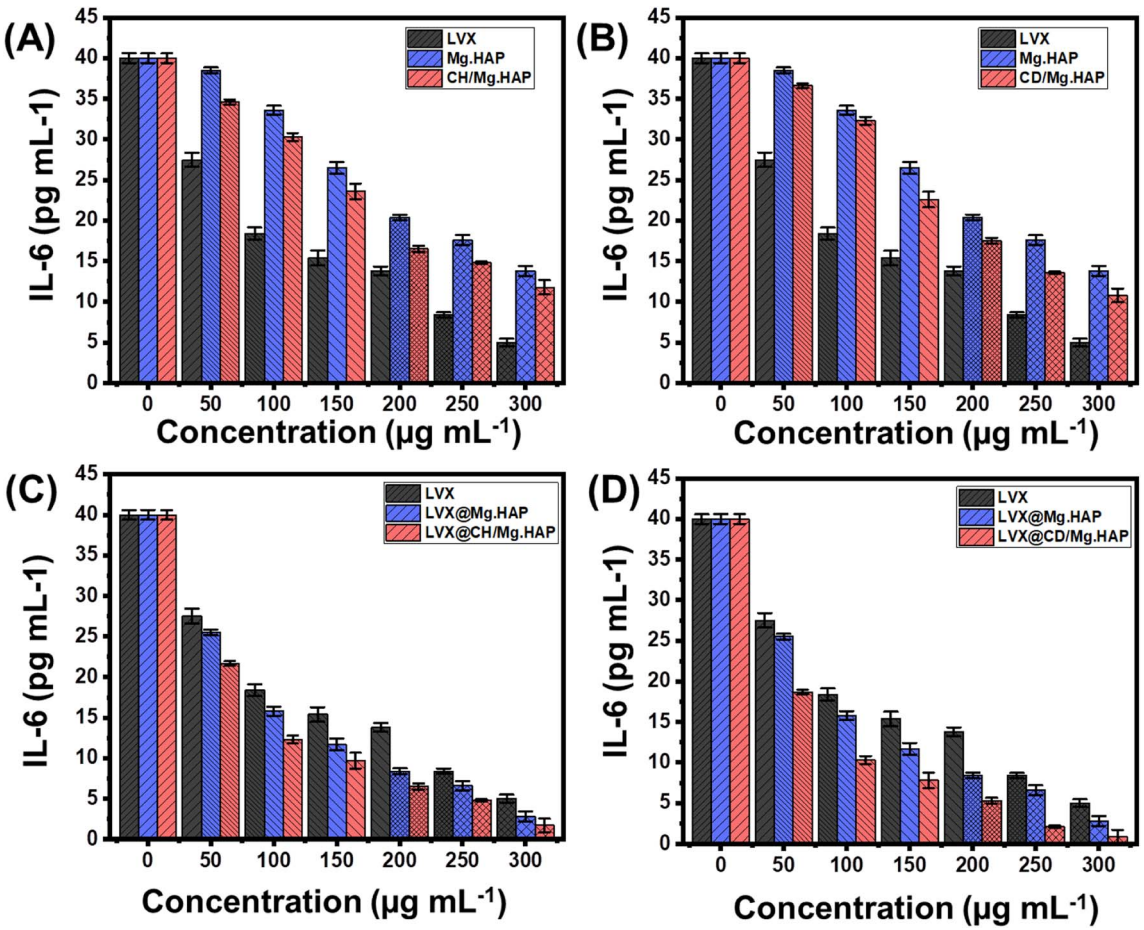

Fig. 8 Influence of free CH/Mg·HAP (A), free CD/Mg·HAP (B), LVX-loaded CD/Mg·HAP (C), and LVX-loaded CD/Mg·HAP (D) in the production of IL-6 proinflammatory cytokines within the NL-20 cells in comparison with free LVX and Mg·HAP.

at a steady rate lower than the initial dose of LVX. Additionally, carriers used must possess sink qualities, and their expansion or solubility show no effect on the pattern of releasing.[23] The Hixson-Crowell model's kinetic concept relies on erosion pathways. Depending on its kinetic theory, the behaviors that are established are significantly influenced by the surface area and grain dimensions of the vehicles.[23,33] The mechanistic theory of Korsmeyer-Peppas suggests that the release processes include both diffusion and erosion pathways that cooperate.[35,73]

The R^2 values show that the releasing procedures of LVX outside the HAP derivatives follow the F-O kinetic model (Fig. 7B) instead of the Z-O kinetic model (Fig. 7A), suggesting that the quantity of loaded LVX significantly affects the release performance. The releasing characteristics match well with both the Higuchi (H-G) (Fig. 7C) and Hixson-Crowell (H-C) (Fig. 7D) theories. The results also verified that the diffusion and erosion processes cooperated throughout the release of LVX. Nevertheless, the releasing behaviors of CH/Mg·HAP and CD/Mg·HAP considerably more closely mimic the Hixson-Crowell kinetics, signifying the essential impacts of the erosion mechanisms. The significant correlation between the release tendencies and the Korsmeyer-Peppas model (Fig. 7E), together with the computed diffusion exponent (n) as a fitting variable, supported the intricate mechanistic theory. The diffusion exponent (n) results are beyond 0.45, suggesting that the releasing processes of LVX from the Mg·HAP, CH/Mg·HAP, and CD/Mg·HAP carriers exhibit non-Fickian transport characteristics (Table 1).[51]

3.5. Anti-inflammatory properties

The effects of free LVX molecules and their loaded forms in Mg·HAP, CH/Mg·HAP, and CD/Mg·HAP on the production of IL-6 and IL-8 in NL20 cells are shown in Fig. 8 and 9. Using LVX as unbound molecules lacking a mediator led to a decrease in the formation of IL-6 and IL-8 generated within the NL20 cells under study (Fig. 8). Moreover, the investigated structures of Mg·HAP, CH/Mg·HAP, and CD/Mg·HAP exhibit slight reduction impacts on the generation of IL-8 and considerable decreasing effects on the production of IL-6, but much lower than the reported influences of the administration of free LVX (Fig. 8). The reducing impact was greatly enhanced by incorporating LVX molecules inside the synthesized Mg·HAP, CH/Mg·HAP, and CD/Mg·HAP nanoparticles as administration vehicles. The generation levels of the IL-6 cytokine diminished by 93%, 95.75%, and 97.85% following the use of LVX@Mg·HAP, LVX@CH/Mg·HAP, and LVX@CD/Mg·HAP at a dose of 300 μg mL^{-1} (Fig. 8). The amount generated of IL-8 cytokine inside NL20 cells decreased by 77.1%, 81.2%, and 85.6% when treated with LVX@Mg·HAP, LVX@CH/Mg·HAP, and LVX@CD/Mg·HAP, respectively, at the identical dose compared with unloaded LVX molecules (Fig. 9). The realized

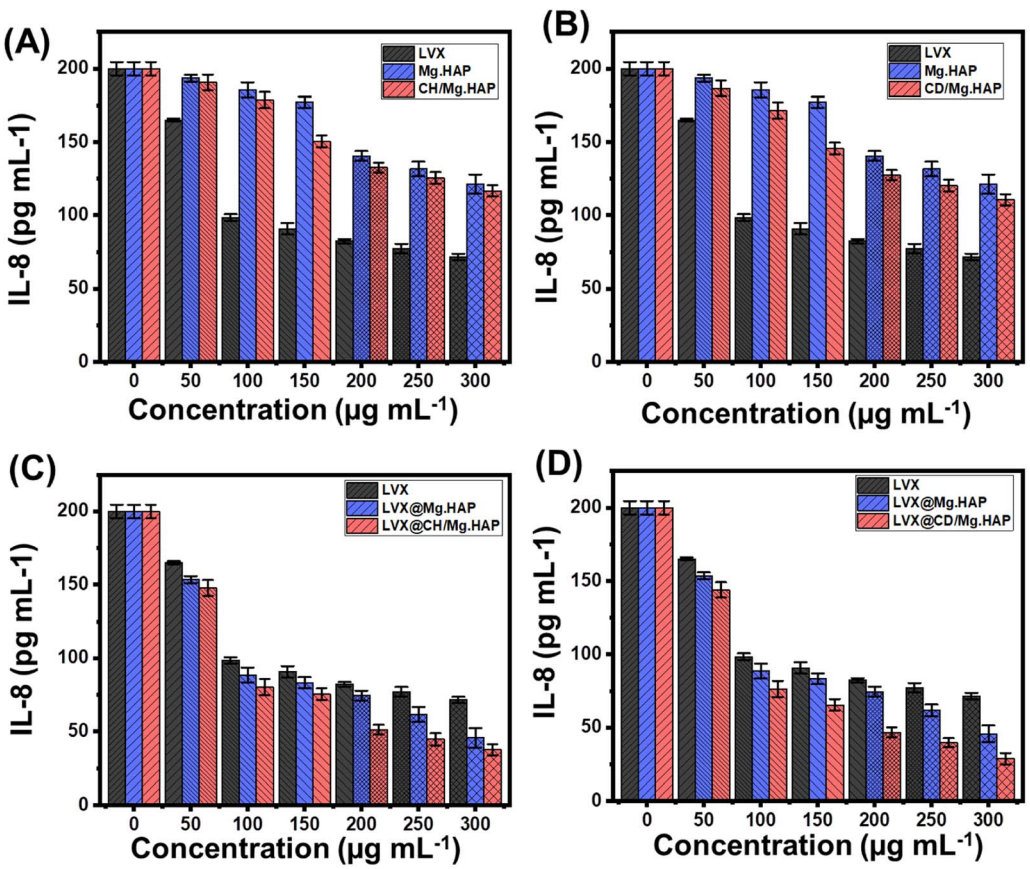

Fig. 9 Influence of free CH/Mg·HAP (A), free CD/Mg·HAP (B), LVX-loaded CD/Mg·HAP (C), and LVX-loaded CD/Mg·HAP (D) in the production of IL-8 proinflammatory cytokines within the NL-20 cells in comparison with free LVX and Mg·HAP.

findings demonstrated the prospective anti-inflammatory qualities of LVX against pro-inflammatory cytokines following its incorporation into the synthesized carriers. Moreover, the implications of the biopolymer integration on inducing the properties of Mg·HAP as carriers of LVX either in terms of the loading and release properties or the anti-inflammatory properties are presented.

3.6. Cytotoxicity properties

The cytotoxic activities of Mg·HAP, CH/Mg·HAP, and CD/Mg·HAP were evaluated prior to and subsequent to the loading of the LVX drug throughout various doses of the composites (100 μg mL^{-1} to 300 μg mL^{-1}). This was conducted according to the cell viability levels reported through the MTT experiment. The cell viability results using Mg·HAP, CH/Mg·HAP, and CD/Mg·HAP lacking LVX demonstrated the remarkable safety and biological compatibility of the synthesized composites as a medication administration method. The highest cell viability values achieved after evaluating the structures at a dose of 300 μg mL^{-1} are 95.2% for Mg·HAP, 92.2% for CH/Mg·HAP, and 90.6% for CD/Mg·HAP.

4. Conclusion

Magnesium-rich hydroxyapatite (Mg·HAP) was synthesized and blended effectively in bio-composites with chitosan (CH/Mg·HAP) and β-cyclodextrin (CD/Mg·HAP) as potential carriers of LVX. CH/Mg·HAP (281.4 mg g^{-1}) and CD/Mg·HAP (332.4 mg g^{-1}) displayed better loading performances than that of Mg·HAP (218.3 mg g^{-1}). The higher density of loading sites of CH/Mg·HAP (115.8 mg g^{-1}) and CD/Mg·HAP (138.5 mg g^{-1}) than that of Mg·HAP (88.03 mg g^{-1}) and enhancement in the organic affinities and surface area illustrate that the loading of LVX is regulated by multi-molecular and physical mechanistic steps considering the loading (<40 kJ mol^{-1}) and Gaussian (<8 kJ mol^{-1}) energies. The composites showed slow release profiles (160 h (CH/Mg·HAP) and 200 h (CD/Mg·HAP)) but were still faster than Mg·HAP. Both diffusion and erosion processes cooperated during the release of LVX based on the kinetic investigation. The anti-inflammatory performance of LVX against the formation of cytokines (IL-6 and IL-8) in the epithelia cells (NL20) was enhanced at a remarkable rate after its loading into Mg·HAP, CH/Mg·HAP, and CD/Mg·HAP, in order.

Conflicts of interest

There are no conflicts to declare.

Acknowledgements

This work was funded by the Deanship of Scientific Research at Princess Nourah Bint Abdulrahman University, through the Research Groups Program Grant no. (RGP-1444-0035)(2).

References

1 L. Schaupp, A. Addante, M. Völler, K. Fentker, A. Kuppe, M. Bardua, J. Duerr, L. Piehler, J. Röhmel, S. Thee, M. Kirchner, M. Ziehm, D. Lauster, R. Haag, M. Gradzielski, M. Stahl, P. Mertins, S. Boutin, S. Y. Graeber and M. A. Mall, Longitudinal effects of elexacaftor/tezacaftor/ivacaftor on sputum viscoelastic properties, airway infection and inflammation in patients with cystic fibrosis, *Eur. Respir. J.*, 2023, **62**, 2202153.

2 L. de O. Macedo, E. J. Barbosa, R. Löbenberg and N. A. Bou-Chacra, Anti-inflammatory drug nanocrystals: state of art and regulatory perspective, *Eur. J. Pharm. Sci.*, 2021, **158**, 105654.

3 H.-K. Wang, Q. Wei, Y.-L. Yang, T.-Y. Lu, Y. Yan and F. Wang, Clinical usefulness of the lymphocyte-to-monocyte ratio and aggregate index of systemic inflammation in patients with esophageal cancer: a retrospective cohort study, *Cancer Cell Int.*, 2023, **23**, 13.

4 Q. Chen, L. Di, Y. Zhang and N. Li, Chemical constituents with cytotoxic and anti-inflammatory activity in Hypericum sampsonii and the antitumor potential under the view of cancer-related inflammation, *J. Ethnopharmacol.*, 2020, **259**, 112948.

5 F. M. Dardir, E. A. Ahmed, M. F. Soliman, S. I. Othman, A. A. Allam, M. A. Alwail and M. R. Abukhadra, Synthesis of chitosan/Al-MCM-41 nanocomposite from natural microcline as a carrier for levofloxacin drug of controlled loading and release properties; Equilibrium, release kinetic, and cytotoxicity, *Colloids Surf., A*, 2021, **624**, 126805.

6 R. Tsivkovskii, M. Sabet, Z. Tarazi, D. C. Griffith, O. Lomovskaya and M. N. Dudley, Levofloxacin reduces inflammatory cytokine levels in human bronchial epithelia cells: implications for aerosol MP-376 (levofloxacin solutionfor inhalation) treatment of chronic pulmonary infections, *FEMS Immunol. Med. Microbiol.*, 2011, **61**, 141–146.

7 S. M. Mahgoub, M. R. Shehata, F. L. Abo El-Ela, A. Farghali, A. Zaher and R. K. Mahmoud, Sustainable waste management and recycling of Zn–Al layered double hydroxide after adsorption of levofloxacin as a safe anti-inflammatory nanomaterial, *RSC Adv.*, 2020, **10**, 27633–27651.

8 A. F. El-Yazbi, K. M. Guirguis, T. S. Belal and M. M. Bedair, Sensitive spectrofluorimetric and mass spectroscopic methods for the determination of nucleic acid damage induced by photosensitized anti-inflammatory drugs: comparative study, *J. Pharm. Biomed. Anal.*, 2020, **187**, 113326.

9 A. S. Khan, A. Iqbal, A. A. Muhammad, F. Mazhar, M. F. Lodhi, K. F. Ahmed, S. Kumar, G. Varrassi and M. Khatri, Safety and Efficacy of Nemonoxacin vs Levofloxacin in Patients With Community-Acquired Pneumonia: A Systematic Review and Meta-Analysis of Randomized Control Trials, *Cureus*, 2023, **52**, 35–44.

10 M. G. Tosato, P. L. Schilardi, M. F. L. de Mele, A. H. Thomas, A. Miñán and C. Lorente, Resveratrol enhancement

staphylococcus aureus survival under levofloxacin and photodynamic treatments, *Int. J. Antimicrob. Agents*, 2018, **51**, 255–259.

11 A. A. Abdelbary, W. H. Abd-Elsalam and A. M. Al-mahallawi, Fabrication of levofloxacin polyethylene glycol decorated nanoliposomes for enhanced management of acute otitis media: statistical optimization, trans-tympanic permeation and in vivo evaluation, *Int. J. Pharm.*, 2019, **559**, 201–209.

12 D. Rungkitwattanakul, W. Chaijamorn, T. Charoensareerat, P. Charntrakarn, O. Khamkampud, N. Rattanaponpasert, N. Srisawat and S. Pattharachayakul, Optimal levofloxacin dosing regimens in critically ill patients with acute kidney injury receiving continuous renal replacement therapy, *J. Crit. Care*, 2021, **63**, 154–160.

13 L. Zhang, L. Tan, Z. Yuan, B. Xu, W. Chen, Y. Tang, L. Li and J. Wang, Engineering of $Bi_2O_2CO_3/Ti_3C_2Tx$ heterojunctions co-embedded with surface and interface oxygen vacancies for boosted photocatalytic degradation of levofloxacin, *Chem. Eng. J.*, 2023, **452**, 139327.

14 X. Zhong, K.-X. Zhang, D. Wu, X.-Y. Ye, W. Huang and B.-X. Zhou, Enhanced photocatalytic degradation of levofloxacin by Fe-doped BiOCl nanosheets under LED light irradiation, *Chem. Eng. J.*, 2020, **383**, 123148.

15 S.-T. Huang, Y.-Q. Lei, P.-R. Guo, W.-X. Zhang, J.-Y. Liang, X. Chen, J.-W. Xu and Z.-H. Diao, Degradation of Levofloxacin by a green zero-valent iron-loaded carbon composite activating peroxydisulfate system: reactivity, products and mechanism, *Chemosphere*, 2023, **340**, 139899.

16 C. Lu, Y. Xiao, Y. Liu, F. Sun, Y. Qiu, H. Mu and J. Duan, Hyaluronic acid-based levofloxacin nanomicelles for nitric oxide-triggered drug delivery to treat bacterial infections, *Carbohydr. Polym.*, 2020, **229**, 115479.

17 M. K. Khang, J. Zhou, C. M. Co, S. Li and L. Tang, A pretargeting nanoplatform for imaging and enhancing anti-inflammatory drug delivery, *Bioact. Mater.*, 2020, **5**, 1102–1112.

18 S. M. Abuzar, E. J. Park, Y. Seo, J. Lee, S. H. Baik and S. J. Hwang, Preparation and evaluation of intraperitoneal long-acting oxaliplatin-loaded multi-vesicular liposomal depot for colorectal cancer treatment, *Pharmaceutics*, 2020, **12**(8), 736.

19 S. Sur, A. Rathore, V. Dave, K. R. Reddy, R. S. Chouhan and V. Sadhu, Recent developments in functionalized polymer nanoparticles for efficient drug delivery system, *Nano-Struct. Nano-Objects*, 2019, **20**, 100397.

20 L. Tian, M. R. Abukhadra, A. S. Mohamed, A. Nadeem, S. F. Ahmad and K. E. Ibrahim, Insight into the loading and release properties of an exfoliated kaolinite/cellulose fiber (EXK/CF) composite as a carrier for oxaliplatin drug: cytotoxicity and release kinetics, *ACS Omega*, 2020, **5**(30), 19165–19173.

21 B. Bayón, V. Bucalá and G. R. Castro, Development of antimicrobial hybrid mesoporous silver phosphate–pectin microspheres for control release of levofloxacin, *Microporous Mesoporous Mater.*, 2016, **226**, 71–78.

22 M. R. Abukhadra, F. A. El Kashief, S. I. Othman, H. A. Alqhtani and A. A. Allam, Synthesis and characterization of Fe0@ chitosan/cellulose biocompatible composites from natural resources as advanced carriers for ibuprofen drug: reaction kinetics and equilibrium, *New J. Chem.*, 2022, **46**(26), 12797–12807.

23 S. I. Othman, A. A. Allam, H. AlFassam, G. M. Abu-Taweel, N. Altoom and M. R. Abukhadra, Sonoco green decoration of clinoptilolite with MgO nanoparticles as a potential carrier for 5-fluorouracil drug: loading behavior, release profile, and cytotoxicity, *Inorg. Organomet. Polym.*, 2021, **31**, 4608–4622.

24 A. M. Itoo, M. Paul, B. Ghosh and S. Biswas, Oxaliplatin delivery via chitosan/vitamin E conjugate micelles for improved efficacy and MDR-reversal in breast cancer, *Carbohydr. Polym.*, 2022, **282**, 119108.

25 I. R. Sayed, A. M. Farhan, A. A. AlHammadi, M. I. El-Sayed, I. M. Abd El-Gaied, A. M. El-Sherbeeny, W. Al Zoubi, Y. G. Ko and M. R. Abukhadra, Synthesis of novel nanoporous zinc phosphate/hydroxyapatite nano-rods (ZPh/HPANRs) core/shell for enhanced adsorption of Ni^{2+} and Co^{2+} ions: characterization and application, *J. Mol. Liq.*, 2022, **360**, 119527.

26 E. Andrew Ofudje, E. F. Sodiya, O. S. Olanrele and F. Akinwunmi, Adsorption of Cd2+ onto apatite surface: equilibrium, kinetics and thermodynamic studies, *Heliyon*, 2023, **9**, e12971.

27 R. Verma, S. R. Mishra, V. Gadore and Md. Ahmaruzzaman, Hydroxyapatite-based composites: excellent materials for environmental remediation and biomedical applications, *Adv. Colloid Interface Sci.*, 2023, **315**, 102890.

28 T. N. Tran, Q. C. Do, J. Kang, J. Kim, J. Kim and S. Kang, Boosted micropollutant removal over urchin-like structured hydroxyapatite-incorporated nickel magnetite catalyst via peroxydisulfate activation, *Water Res.*, 2024, **249**, 120951.

29 S.-M. Huang, W.-C. Chen, C.-C. Wu, S.-M. Liu, C.-L. Ko, J.-C. Chen and C.-J. Shih, Synergistic effect of drug/antibiotic-impregnated micro/nanohybrid mesoporous bioactive glass/calcium phosphate composite bone cement on antibacterial and osteoconductive activities, *Biomater. Adv.*, 2023, **152**, 213524.

30 E. W. Elsayed, A. A. El-Ashmawy, G. T. El-Bassyouni, S. M. Mousa, M. El-Manawaty and L. H. Emara, Formulation and evaluation of alginate-gelatin hydrogel scaffolds loaded with zinc-doped hydroxyapatite and 5-fluorouracil, *Int. J. Biol. Macromol.*, 2023, **237**, 124147.

31 N. Salahuddin, E. M. Ibrahim and M. El-Kemary, Different methods for preparation of hydroxyapatite nanostructures, *Biointerface Res. Appl. Chem.*, 2023, **13**, 236.

32 A. M. Saad, M. R. Abukhadra, S. Abdel-Kader Ahmed, A. M. Elzanaty, A. H. Mady, M. A. Betiha, J.-J. Shim and A. M. Rabie, Photocatalytic degradation of malachite green dye using chitosan supported ZnO and Ce–ZnO nano-flowers under visible light, *J. Environ. Manage.*, 2020, **258**, 110043.

33 S. M. Ibrahim, M. N. Bin Jumah, S. I. Othman, R. S. Alruhaimi, N. Al-Khalawi, Y. F. Salama, A. A. Allam and M. R. Abukhadra, Synthesis of Chitosan/Diatomite

Composite as an Advanced Delivery System for Ibuprofen Drug; Equilibrium Studies and the Release Profile, *ACS Omega*, 2021, **6**, 13406–13416.

34 Y. Jiang, M. R. Abukhadra, N. M. Refay, M. F. Sharaf, M. A. El-Meligy and E. M. Awwad, Synthesis of chitosan/MCM-48 and β-cyclodextrin/MCM-48 composites as bio-adsorbents for environmental removal of Cd2+ ions; kinetic and equilibrium studies, *React. Funct. Polym.*, 2020, **154**, 104675.

35 H. M. El-Zeiny, M. R. Abukhadra, O. M. Sayed, A. H. Osman and S. A. Ahmed, Insight into novel β-cyclodextrin-grafted poly (Nvinylcaprolactam) nanogel structures as advanced carriers for 5- fluorouracil: equilibrium behavior and pharmacokinetic modeling, *Colloids Surf., A*, 2020, **586**, 124197.

36 S. Sadjadi and F. Koohestani, Composite of β-cyclodextrin and bentonite clay: a promising support for Pd immobilization and developing a catalyst for hydrogenation of nitroarenes under mild reaction condition, *J. Phys. Chem. Solids*, 2021, **151**, 109894.

37 K. Krawczyk, D. Silvestri, N. H. A. Nguyen, A. Ševců, D. Łukowiec, V. V. Padil, M. Řezanka, M. Černík, D. D. Dionysiou and S. Wacławek, Enhanced degradation of sulfamethoxazole by a modified nano zero-valent iron with a β-cyclodextrin polymer: mechanism and toxicity evaluation, *Sci. Total Environ.*, 2022, **817**, 152888.

38 A. M. El-Sherbeeny, S. M. Ibrahim, A. A. AlHammadi, A. T. A. Soliman, J. J. Shim and M. R. Abukhadra, Effective retention of radioactive Cs^{+} and Ba^{2+} ions using β-cyclodextrin functionalized diatomite (β-CD/D) as environmental adsorbent; characterization, application, and safety, *Surf. Interfaces*, 2021, **26**, 101434.

39 M. N. B. Jumah, M. H. Eid, A. A. AL-Huqail, M. A. Mohammad, N. S. Bin-Murdhi, G. M. Abu-Taweel, N. Altoom, A. A. Allam and M. R. AbuKhadra, Enhanced remediation of As (V) and Hg (II) ions from aqueous environments using β-cyclodextrin/MCM-48 composite: batch and column studies, *J. Water Process Eng.*, 2021, **42**, 102118.

40 P. Saokham, C. Muankaew, P. Jansook and T. Loftsson, Solubility of cyclodextrins and drug/cyclodextrin complexes, *Molecules*, 2018, **23**(5), 1161.

41 A. T. Okasha, A. A. Abdel-Khalek, A. M. El-Sherbeeny, W. Al Zoubi and M. R. Abukhadra, Advanced equilibrium study on the synthesis and characterization of Mg-doped hydroxyapatite nano-fibers as a potential enhanced adsorbent of Zn (II) and malachite green dye, *Mater. Today Commun.*, 2023, 105883.

42 N. Altoom, S. M. Ibrahim, S. I. Othman, A. A. Allam, H. A. Alqhtani, F. S. Al-Otaibi and M. R. Abukhadra, Characterization of β-cyclodextrin/phillipsite (β-CD/Ph) composite as a potential carrier for oxaliplatin as therapy for colorectal cancer; loading, release, and cytotoxicity, *Colloids Surf., A*, 2022, **648**, 129144.

43 Y. Zhou, W. Li, X. Jiang, Y. Sun, H. Yang, Q. Liu, Y. Cao, Y. Zhang and H. Cheng, Synthesis of strontium (Sr) doped hydroxyapatite (HAp) nanorods for enhanced adsorption of Cr (VI) ions from wastewater, *Ceram. Int.*, 2021, **47**(12), 16730–16736.

44 L. Fan, W. Kong, C. Gao and P. Zhu, Synthesis of highly porous iron-doped carbonated hydroxyapatite spheres for efficient adsorption of carmine dyes, *Materialia*, 2021, **20**, 101205.

45 T. Xiong, Q. Li, J. Liao, Y. Zhang and W. Zhu, Highly enhanced adsorption performance to uranium (VI) by facile synthesized hydroxyapatite aerogel, *J. Hazard. Mater.*, 2022, **423**, 127184.

46 R. Foroutan, S. J. Peighambardoust, A. Ahmadi, A. Akbari, S. Farjadfard and B. Ramavandi, Adsorption mercury, cobalt, and nickel with a reclaimable and magnetic composite of hydroxyapatite/Fe_3O_4/polydopamine, *J. Environ. Chem. Eng.*, 2021, **9**(4), 105709.

47 Y. Liu, C. Dong, H. Wei, W. Yuan and K. Li, Adsorption of levofloxacin onto an iron-pillared montmorillonite (clay mineral): kinetics, equilibrium and mechanism, *Appl. Clay Sci.*, 2015, **118**, 301–307.

48 Y. Xiang, Z. Xu, Y. Zhou, Y. Wei, X. Long, Y. He, D. Zhi, J. Yang and L. Luo, A sustainable ferromanganese biochar adsorbent for effective levofloxacin removal from aqueous medium, *Chemosphere*, 2019, **237**, 124464.

49 X. Qin, P. Du, J. Chen, F. Liu, G. Wang and L. Weng, Effects of natural organic matter with different properties on levofloxacin adsorption to goethite: experiments and modeling, *Chem. Eng. J.*, 2018, **345**, 425–431.

50 Q. Ma, H. Zhang, X. Zhang, B. Li, R. Guo, Q. Cheng and X. Cheng, Synthesis of magnetic CuO/MnFe2O4 nanocompisite and its high activity for degradation of levofloxacin by activation of persulfate, *Chem. Eng. J.*, 2019, **360**, 848–860.

51 M. R. Abukhadra, N. M. Refay, A. Nadeem, A. M. El-Sherbeeny and K. E. Ibrahim, Insight into the role of integrated carbohydrate polymers (starch, chitosan, and β-cyclodextrin) with mesoporous silica as carriers for ibuprofen drug; equilibrium and pharmacokinetic properties, *Int. J. Biol. Macromol.*, 2020, **156**, 537–547.

52 M. Salam, M. Mokhtar, S. M. Albukhari, D. F. Baamer, L. Palmisano, M. Jaremko and M. R. Abukhadra, Synthesis and Characterization of Green ZnO@ polynaniline/Bentonite Tripartite Structure (G. Zn@ PN/BE) as Adsorbent for As (V) Ions: Integration, Steric, and Energetic Properties, *Polymers*, 2022, **14**(12), 2329.

53 M. A. Salam, M. R. Abukhadra and M. Mostafa, Effective decontamination of As (V), Hg (II), and U (VI) toxic ions from water using novel muscovite/zeolite aluminosilicate composite: adsorption behavior and mechanism, *Environ. Sci. Pollut. Res.*, 2020, **27**(12), 13247–13260.

54 E. El Qada, Kinetic Behavior of the Adsorption of Malachite Green Using Jordanian Diatomite as Adsorbent, *Jordanian J. Eng. Chem. Ind.*, 2020, **3**(1), 1–10.

55 X. Lin, Y. Xie, H. Lu, Y. Xin, R. Altaf, S. Zhu and D. Liu, Facile preparation of dual La-Zr modified magnetite adsorbents for efficient and selective phosphorus recovery, *Chem. Eng. J.*, 2021, **413**, 127530.

56 S. M. Albukhari, M. A. Salam and M. R. Abukhadra, Effective retention of inorganic Selenium ions (Se (VI) and Se (IV)) using novel sodalite structures from muscovite; characterization and mechanism, *J. Taiwan Inst. Chem. Eng.*, 2021, **120**, 116–126.

57 A. Sherlala, M. M. Raman and A. Bello, Buthiyappan, Adsorption of arsenic using chitosan magnetic graphene oxide nanocomposite, *J. Environ. Manage.*, 2019, **246**, 547–556.

58 Y. Huang, X. Zeng, L. Guo, J. Lan, L. Zhang and D. Cao, Heavy metal ion removal of wastewater by zeolite-imidazolate frameworks, *Sep. Purif. Technol.*, 2018, **194**, 462–469.

59 E. E. Jasper, V. O. Ajibola and J. C. Onwuka, Nonlinear regression analysis of the sorption of crystal violet and methylene blue from aqueous solutions onto an agro-waste derived activated carbon, *Appl. Water Sci.*, 2020, **10**(6), 1–11.

60 F. Dawodu, G. Akpomie and M. Abuh, Equilibrium Isotherm Studies on the Batch Sorption of Copper (II) ions from Aqueous Solution unto Nsu Clay, *Int. J. Sci. Eng. Res.*, 2012, **3**(12), 1–7.

61 X. Yang, J. Wang, A. M. El-Sherbeeny, A. A. AlHammadi, W. H. Park and M. R. Abukhadra, Insight into the adsorption and oxidation activity of a ZnO/piezoelectric quartz core-shell for enhanced decontamination of ibuprofen: steric, energetic, and oxidation studies, *Chem. Eng. J.*, 2022, **431**, 134312.

62 L. Sellaoui, H. Guedidi, L. Reinert, S. Knani, L. Duclaux and A. B. Lamine, Experimental and theoretical studies of adsorption of ibuprofen on raw and two chemically modified activated carbons: new physicochemical interpretations, *RSC Adv.*, 2016, **6**(15), 12363–12373.

63 R. A. Ali, M. Mobarak, A. M. Badawy, E. C. Lima, M. K. Seliem and H. S. Ramadan, New insights into the surface oxidation role in enhancing Congo red dye uptake by Egyptian ilmenite ore: experiments and physicochemical interpretations, *Surf. Interfaces*, 2021, **26**, 101316.

64 M. T. Ashraf, A. A. AlHammadi, A. M. El-Sherbeeny, S. Alhammadi, W. Al Zoubi, Y. G. K. Supervison and M. R. Abukhadra, Synthesis of cellulose fibers/Zeolite-A nanocomposite as an environmental adsorbent for organic and inorganic selenium ions; characterization and advanced equilibrium studies, *J. Mol. Liq.*, 2022, **360**, 119573.

65 M. Mostafa, M. A. El-Meligy, M. Sharaf, A. T. Soliman and M. R. AbuKhadra, Insight into chitosan/zeolite-A nanocomposite as an advanced carrier for levofloxacin and its anti-inflammatory properties; loading, release, and anti-inflammatory studies, *Int. J. Biol. Macromol.*, 2021, **179**, 206–216.

66 J. Wang, N. Cai, V. Chan, H. Zeng, H. Shi, Y. Xue and F. Yu, Antimicrobial hydroxyapatite reinforced-polyelectrolyte complex nanofibers with long-term controlled release activity for potential wound dressing application, *Colloids Surf., A*, 2021, **624**, 126722.

67 K. AbouAitah, M. Bil, E. Pietrzykowska, U. Szałaj, D. Fudala, B. Woźniak, J. Nasiłowska, A. Swiderska-Sroda, M. Lojkowski, B. Sokołowska and W. Swieszkowski, Drug-Releasing Antibacterial Coating Made from Nano-Hydroxyapatite Using the Sonocoating Method, *Nanomaterials*, 2021, **11**(7), 1690.

68 A. N. Elboraey, H. H. Abo-Almaged, A. A. E. R. El-Ashmawy, A. R. Abdou, A. R. Moussa, L. H. Emara, H. M. El-Masry, G. E. T. El Bassyouni and M. I. Ramzy, Biological and mechanical properties of denture base material as a vehicle for novel hydroxyapatite nanoparticles loaded with drug, *Adv. Pharm. Bull.*, 2021, **11**(1), 86.

69 M. A. Sayed, H. M. El-Zeiny, J. S. Khim, J. S. Ajarem, A. A. Allam and M. R. Abukhadra, Insight into the loading properties of Na+ green functionalized clinoptilolite as a potential carrier for the 5-fluorouracil drug, its release kinetics, and cytotoxicity, *ACS Omega*, 2022, **7**(8), 6991–7001.

70 F. Rehman, K. Ahmed, A. Rahim, N. Muhammad, S. Tariq, U. Azhar, A. J. Khan, Z. Sama, P. L. Volpe and C. Airoldi, Organo-bridged silsesquioxane incorporated mesoporous silica as a carrier for the controlled delivery of ibuprofen and fluorouracil, *J. Mol. Liq.*, 2018, **258**, 319–326.

71 P. Sundaramoorthy, T. Ramasamy, S. K. Mishra, K. Y. Jeong, C. S. Yong, J. O. Kim and H. M. Kim, Engineering of caveolae-specific self-micellizing anticancer lipid nanoparticles to enhance the chemotherapeutic efficacy of oxaliplatin in colorectal cancer cells, *Acta Biomater.*, 2016, **42**, 220–231.

72 M. Ge, W. Tang, M. Du, G. Liang, G. Hu and S. J. Alam, Research on 5-fluorouracil as a drug carrier materials with its in vitro release properties on organic modified magadiite, *Eur. J. Pharm. Sci.*, 2019, **130**, 44–53.

73 H. El-Hamshary, M. H. El-Newehy, M. Moydeen Abdulhameed, A. ElFaham and A. S. Elsherbiny, Evaluation of clay-ionene nanocomposite carriers for controlled drug delivery: synthesis, in vitro drug release, and kinetics, *Mater. Chem. Phys.*, 2019, **225**, 122–132.